Adsorption geometry and electronic structure of a charge-transfer-complex: TTF-PYZ_2 on Ag(110)

To cite this article before publication: Patrick Kretz *et al* 2020 *New J. Phys.* in press https://doi.org/10.1088/1367-2630/abcace

Adsorption geometry and electronic structure of a charge-transfer-complex: TTF-PYZ_2 on Ag(110)

Patrick Kretz,[1] Kay Waltar,[1] Yan Geng,[2,*] Christian Metzger,[3] Martin Graus,[3] Achim Schöll,[3] Friedrich Reinert,[3] Shi-Xia Liu,[2] Silvio Decurtins,[2] Matthias Hengsberger,[1] Jürg Osterwalder,[1] and Luca Castiglioni[1,†]

[1] *Physics Department, University of Zurich, 8057 Zurich, Switzerland*

[2] *Chemistry Department, University of Bern, 3012 Bern, Switzerland*

[3] *Experimental Physics VII, University of Würzburg, 97074 Würzburg, Germany*

(Dated: November 9, 2020)

Abstract

We study electronic properties and adsorption geometries of the molecular charge-transfer-complex tetrathiafulvalene-dipyrazine on Ag(110). Using a combination of angle-resolved photoemission and electron diffraction, supported by DFT-based simulations, renders a comprehensive picture of this interesting system. We find low interaction between the substrate and the molecule and thus little changes of the molecular geometry upon adsorption, as compared to the free gas phase molecule. Five electronic valence states can be unambiguously assigned owing to their distinctive photoemission patterns. The molecules adsorb aligned with the Ag rows in the first layer, while they are slightly rotated in the second layer. Additional intensity of the molecular photoemission signal near the Fermi energy indicates partial charge-transfer into formerly unoccupied states, most likely of intermolecular origin.

* Present Address: College of Chemistry, Chemical Engineering and Material Science, Shandong Normal University, Jinan 250014, P. R. China

† castiglioni@physik.uzh.ch

I. INTRODUCTION

Charge-transfer complexes (CTC) have been widely studied since the discovery of the first organic metal TTF-TCNQ (tetrathiofulvalene-tetracyanoquinodimethane) in 1973 [1] and even superconductivity in a similar compound [2]. Such materials are made up by crystal structures combining electron donating (D) and electron accepting (A) molecules. The electronic coupling between the molecules leads to partial charge transfer between the highest occupied molecular orbital (HOMO) of the donor and the lowest unoccupied molecular orbital (LUMO) of the acceptor. The CTCs can exhibit properties very different from their parent compounds, such as photoconductivity, field emission, rectification, photo-switch or memory function and are thus of high technological interest [3–6].

Fused D-A systems, where the electron donating and accepting entities are part of the same molecule, have attracted special attention during the past decades [7] due to their potential application in photovoltaic devices [8] and organic semiconductors and conductors [9]. Tetrathiafulvalene-dipyrazine (TTF-PYZ_2) is a compactly fused ambipolar CTC which was first synthesized in 2011 [10]. The covalently linked A-D-A array leads to an interesting electronic structure. The main characteristics displayed in Fig.1 are the HOMO located on the TTF center and the LUMO on the PYZ wings of the molecule. These states are separated by a relatively small band gap of 2.39 eV [10]. Such compactly fused D-A systems are known to show photoinduced charge-transfer and long-lived charge-separated states [11–13].

Schuler et al. studied the adsorption of TTF-PYZ_2 on a NaCl-bilayer on Cu(111) by means of Kelvin-probe-force microscopy [14]. They found two different adsorption structures (conformations) on the NaCl surface. In the first conformation, the TTF part is close to the substrate while the PYZ wings are bent away from the surface plane (compare Fig 1(a) bottom). In the second structure the wings are bent towards the surface. In their DFT simulation of the free molecule, they found a bending angle of 12°, which is very close to the angle of 13.5° measured in bare TTF by electron diffraction. The symmetry of the bent molecular geometry is reduced from a D_{2h} to a C_{2v} point group symmetry.

In this work, we study TTF-PYZ_2 adsorbed on an Ag(110) substrate. We employ a combination of orbital tomography based on angle-resolved photoelectron spectroscopy (ARPES) [15–18], low-energy electron diffraction (LEED) and DFT simulations to determine adsorp-

tion geometry and the molecular electronic structure. In the absence of final state scattering, when the photoemission signal is recorded from a well-ordered monolayer or multilayer of organic molecules consisting of light atoms (H, C, N, O), a plane wave can be used to describe the photoemission final state [15, 19, 20]. In this case, the photoelectron momentum distribution corresponds to the Fourier transform of the initial state, i. e. the molecular orbital, which can be directly reconstructed via iterative phase-retrieval algorithms [15, 17, 21, 22]. To overcome the limitations of the plane-wave approximation, we simulate the experimental photoelectron momentum distributions based on the independent-atomic-centre (IAC) approximation. This approximation is a versatile and generally applicable theory to calculate angular photoemission from molecules [23, 24]. In contrast to the plane wave approximation, the IAC approximation is not restricted to any molecular geometry nor orbital character.

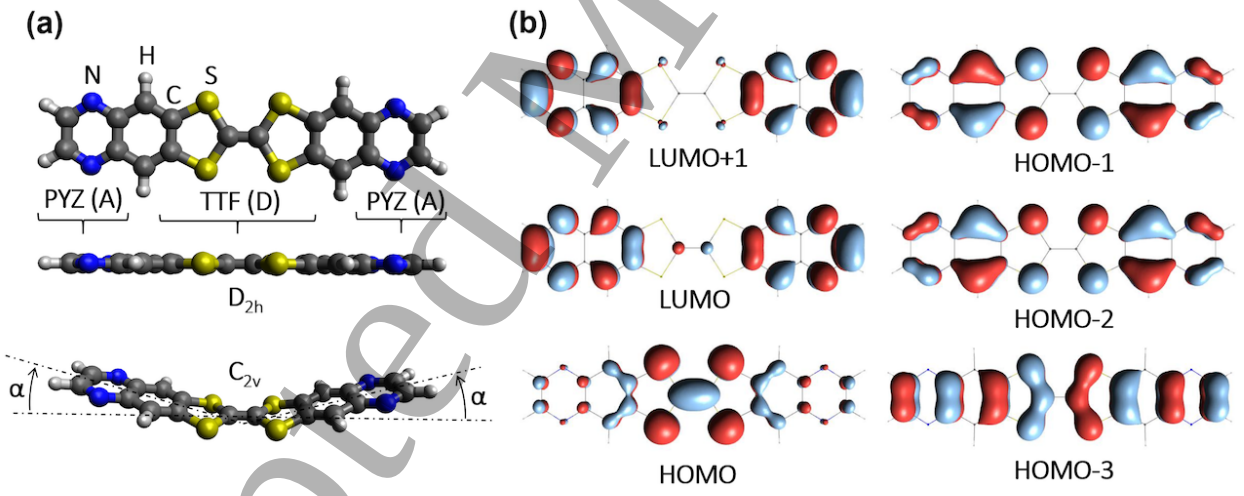

FIG. 1. Geometry and molecular orbitals of TTF-PYZ_2. (a) Enforced planar D_{2h} symmetry (top) and the fully relaxed, bent C_{2v} configuration (bottom). The central TTF part with donor (D) functionality is surrounded by two PYZ moieties with acceptor (A) functionality. (b) Frontier molecular orbitals in D_{2h} symmetry. The bent geometry has almost the same electronic structure and is thus not shown.

II. METHODS

A. Sample preparation, LEED and ARPES measurements

All experiments were carried out in an ultra-high vacuum (UHV) system consisting of a preparation chamber and an analysis chamber with a base pressure $< 10^{-10}$ mbar [25]. The Ag(110) single crystal was prepared by repeated cycles of Ar^+ sputtering and annealing. Highly-ordered molecular films on Ag(110) were grown by effusing TTF-PYZ_2 molecules from home-built Knudsen cell-type evaporators. Both substrate surface cleanliness and quality of the molecular films were verified by LEED and x-ray photoelectron spectroscopy (XPS). Coverage was estimated from LEED and further verified by XPS, which was also used to confirm the stoichiometry and thus structural integrity of the adsorbed molecules. The angle-resolved photoemission data was collected by a two-dimensional wide-angle electron energy analyzer with He I_α radiation (21.2 eV) from a discharge lamp as excitation source. The sample is attached to a rotatable manipulator, while the light source and the electron analyzer are mounted to the UHV chamber. By rotating the sample around the polar angle θ (range: 0°-90°) and the azimuthal angle φ (range: 0°-360°) the full hemisphere above the sample can be scanned. The measurement geometry including the definition of a coordinate system and the angles is depicted in Fig 2. The single detector images were processed to complete photoelectron momentum maps (PMM) according to our previously published routines [25]. ARPES data for PMMs is typically integrated over an energy range of 0.2 eV.

B. Photoemission calculations

The photoemission intensity is derived from Fermi's Golden Rule that describes the probability for a transition from an initial state into a final state which is characterised by its momentum $\boldsymbol{k}$. Accordingly, the total photoemission intensity measured as a function of E_{kin} at a polar angle θ and an azimuthal angle φ is proportional to the sum over all occupied electronic initial states:

$$I(\theta, \varphi; E_{kin}) \propto \sum_i |\langle \psi_f(\theta, \varphi; E_{kin}) | \boldsymbol{\epsilon} \cdot \boldsymbol{r} | \psi_i \rangle|^2 \times \delta(E_i + \phi + E_{kin} - h\nu) \quad (1)$$

Within the plane wave approximation where ψ_f is represented by a plane wave, the mea-

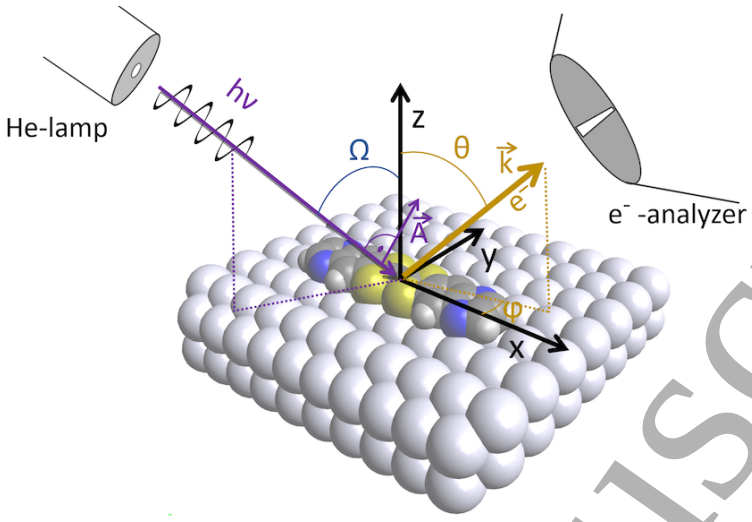

FIG. 2. Geometry of the ARPES experiment. The incidence angle of the light, Ω, changes during the measurement. The orientation of the sample surface with respect to the detection axis of the electron analyzer is given by the polar and azimuthal angles, θ and φ, respectively

sured photoemission intensity becomes proportional to the squared modulus of the Fourier transform of the initial state wave function ψ_i [15]. In the independent-atomic-centre (IAC) approximation [26–28] the initial state is decomposed into the atomic orbitals

$$\psi_i(\boldsymbol{r}) = \sum_{\alpha} \sum_{nlm} C_{\alpha,nlm} \phi_{\alpha,nlm}(\boldsymbol{r} - \boldsymbol{R}_\alpha) \tag{2}$$

positioned at $\mathbf{R}_\alpha$ and the final state is expressed as Coulomb waves $\propto R_{kl}(R) Y_{LM}(\hat{\mathbf{R}})$ with energy E_{kin}, where Y_{LM} is the angular part given by the spherical harmonics. Computing the resulting sum leads to the IAC expression for the final state wave function, ψ_{IAC}, at the detector position $\mathbf{R}$:

$$\psi_{\mathrm{IAC}}(\boldsymbol{R}, E_{kin}) = \sum_{\alpha} \sum_{nlm} C_{\alpha,nlm} e^{i\boldsymbol{k}\boldsymbol{R}_\alpha} \sum_{LM} M^{LM}_{nlm}(E_{kin}) Y_{LM}(\hat{\mathbf{R}}) \tag{3}$$

The square of the wave function is proportional to the intensity at the detector position. M^{LM}_{nlm} is the matrix element and L, M the angular momentum quantum numbers of the Coulomb waves. The IAC code that was used in previous work [29] has been adapted to account for the different experimental geometry. The refraction of the photoelectron wave at the solid vacuum interface can be described by the change in kinetic energy, which is quantified by the so-called inner potential, V_0, representing the zero of the kinetic energy

inside the solid. This value V_0 was used as a fitting parameter and was found to be ~7 eV. The initial state wave functions, ψ_i, and other molecular properties of TTF-PYZ_2 were obtained from DFT calculations using Gaussian 09 [30] at the B3LYP/6-31G+ level of theory.

III. RESULTS AND DISCUSSION

A. LEED analysis and surfaces lattices of TTF-PYZ_2 on Ag(110)

TTF-PYZ_2 forms a long-range ordered superstructure on Ag(110). The LEED data is shown in Fig. 3 together with the deduced real space structures. For one monolayer (ML, Fig. 3(a)), the superstructure is commensurate and the relation between the Ag(110) lattice vectors $\mathbf{a}_1$ and $\mathbf{a}_2$ and the superstructure lattice vectors $\mathbf{b}_1$ and $\mathbf{b}_2$ can be expressed by a matrix G_{ML} and the following relation:

$$\begin{pmatrix}\mathbf{b}_1\\ \mathbf{b}_2\end{pmatrix} = \underbrace{\frac{1}{2}\begin{pmatrix}13 & 2\\ 1 & 4\end{pmatrix}}_{G_{ML}}\begin{pmatrix}\mathbf{a}_1\\ \mathbf{a}_2\end{pmatrix}. \quad (4)$$

There are two equivalent mirror-symmetric domains with the mirror axis parallel to the Ag rows ($[1\bar{1}0]$-direction). The densely packed structure and size of the molecule suggest single orientation. The fact that the distance along $[1\bar{1}0]$ is so short suggests a bent adsorption geometry, which reduces the overlap between adjacent molecules.

The work function of the surface decreases from 4.2 eV to 3.7 eV upon adsorption of 1.0 monolayer (ML). This decrease is probably caused by the molecular dipole reducing the surface dipole and thereby also the work function, a common effect of molecules adsorbed on surfaces [31].

Upon further evaporation onto the ML an additional structure becomes visible in the LEED images. This structure is assigned to the ordering of the second TTF-PYZ_2 layer and is indicated in Fig. 3(b). No further shift of the work function is observed.

The second layer structure (Fig. 3(c)) can be described in real space by the Matrix G_{BL} and the relation

$$\begin{pmatrix}\mathbf{c}_1\\ \mathbf{c}_2\end{pmatrix} = \underbrace{\frac{1}{18}\begin{pmatrix}-69 & -18\\ 124 & -18\end{pmatrix}}_{G_{BL}}\begin{pmatrix}\mathbf{a}_1\\ \mathbf{a}_2\end{pmatrix} \quad (5)$$

between the substrate unit cell vectors $\mathbf{a}_1$ and $\mathbf{a}_2$ and the second layer unit cell vectors $\mathbf{c}_1$ and $\mathbf{c}_2$.

The molecules in the second layer are even more densely packed than in the first layer ($\det(G_{BL}) = 10.9$ compared to $\det(G_{ML}) = 12.5$). From the close packing and the size of the TTF-PYZ_2 molecule it is assumed, that the long axis is rotated relative to the first layer molecules and to the Ag rows by ideally 11.6° around azimuthal. This rotation minimizes the overlap and is shown in Fig. 3(e). As in the first layer, there are two mirror symmetric domains. In the following, we will verify our assumptions on the molecular geometry by taking a closer look at the ARPES data of the molecular valence states.

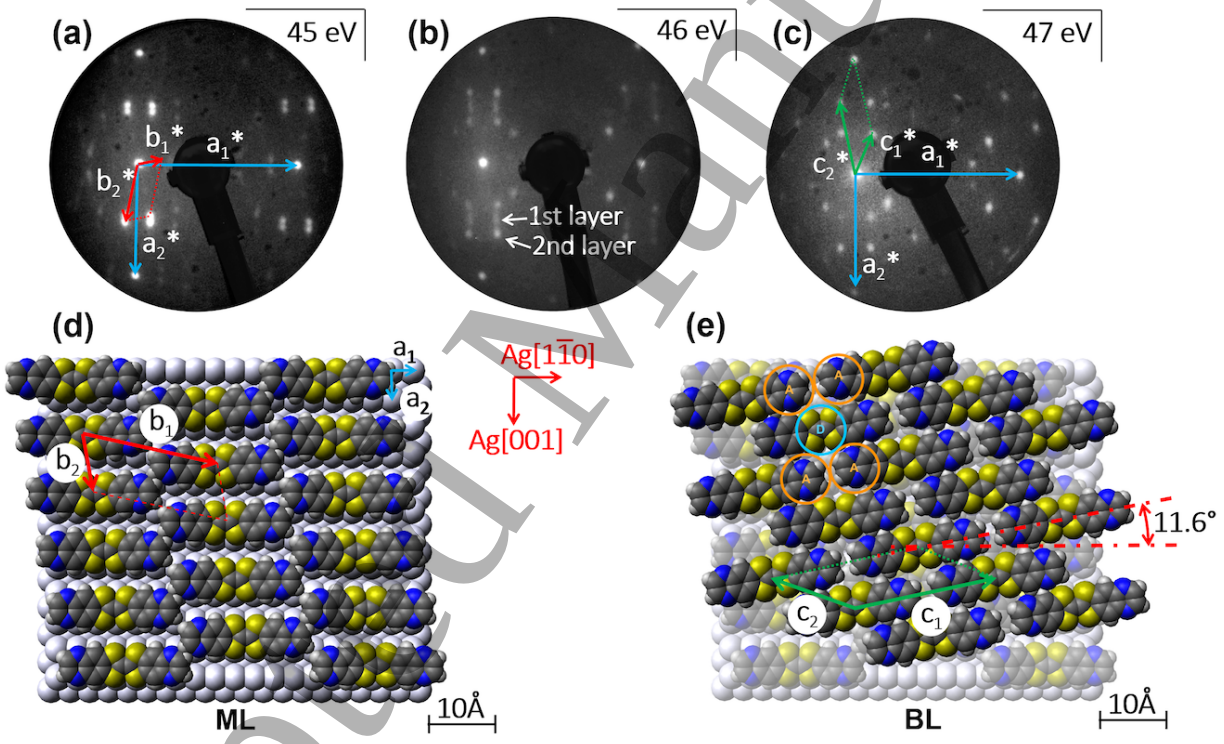

FIG. 3. LEED analysis. (a) LEED image of a monolayer (ML) with reciprocal 2d lattice vectors of Ag(110) surface (blue) and superstructure (red). (b) LEED image of intermediate coverage (≈ 1.5 ML) with spots of the first and second adlayers. (c) LEED image of a bilayer with reciprocal 2d lattice vectors of the 2nd layer superstructure (green). (d-e) Real space structures of the first and second layer along with the real space 2d lattice vectors. The azimuthal rotation of the second layer molecules, facilitating interaction between A and D functionalities of neighbouring molecules, is indicated in (e).

B. ARPES data

Figure 4(a) shows the ultraviolet photoelectron spectrum (UPS) of a monolayer (ML) and a bilayer (BL) of TTF-PYZ_2 on Ag(110). We note that the energetic positions of the main molecular features (2.2 eV and 3.6 eV) are the same for the ML and BL. While there is no peak discernible at 3.0 eV, we observe distinctive features in the complete photoelectron momentum map (PMM) that resemble molecular features in this binding energy range (see Fig. 5). We assume the energetically highest occupied state to be the HOMO. The PMMs of this state are shown in Figs. 4(c) and (c) for the ML and BL, respectively. We now focus on the intensity maxima at $k_x = \pm$ 1.5 Å^{-1} ($k_y = 0$). This feature seems slightly wider in case of the BL. This becomes more evident looking at the intensity profiles from a horizontal cut through the feature (Fig. 4(d)). The observed widening in case of the BL can be rationalised by considering the azimuthal rotation of the molecules in the second layer, as already suggested from the LEED data. The observed PMM can then be considered the incoherent sum of HOMO emission from the two rotational domains in the BL and some attenuated contribution of the first layer (ML) beneath. A PMM of the clean Ag(110) substrate at the same binding energy is shown for comparison (Fig. 4(e)). In all shown PMMs, the vertical mirror symmetry is broken due to the oblique incidence angle of the light, which is not in the symmetry planes of the experiment (xy and yz, *cf.* Fig. 2).

We employ simulations based on the independent-atomic-centre (IAC) approximation to compare our electronic structure calculations of TTF-PYZ_2 with the ARPES data. Figure 5 shows a comparison of the PMMs of all observed valence states with IAC simulations. The lowest observable feature before the onset of the Ag substrate d-bands at 3.6 eV can be assigned to the TTF-PYZ_2 HOMO-3 (Fig. 5(a)). The PMM at 3.0 eV in Fig. 5(b) contains contributions from two energetically close-lying states, the HOMO-2 and HOMO-1. The real space wave functions are depicted next to the simulations. The experimental PMM can be well reproduced by the incoherent sum of those two states. Finally, the HOMO data is shown in Fig. 5(c). The additional features in the HOMO-3 experimental data that are not present in the simulations can be attributed to some residual overlap with HOMO-2. Both HOMO-3 and HOMO exhibit the same parity (i. e. the same irreducible representation) and thus also have a similar PMMs. The main difference lies in the k_x value of the main feature due to the different periodicity of the wave functions along the x-axis. This is highlighted in

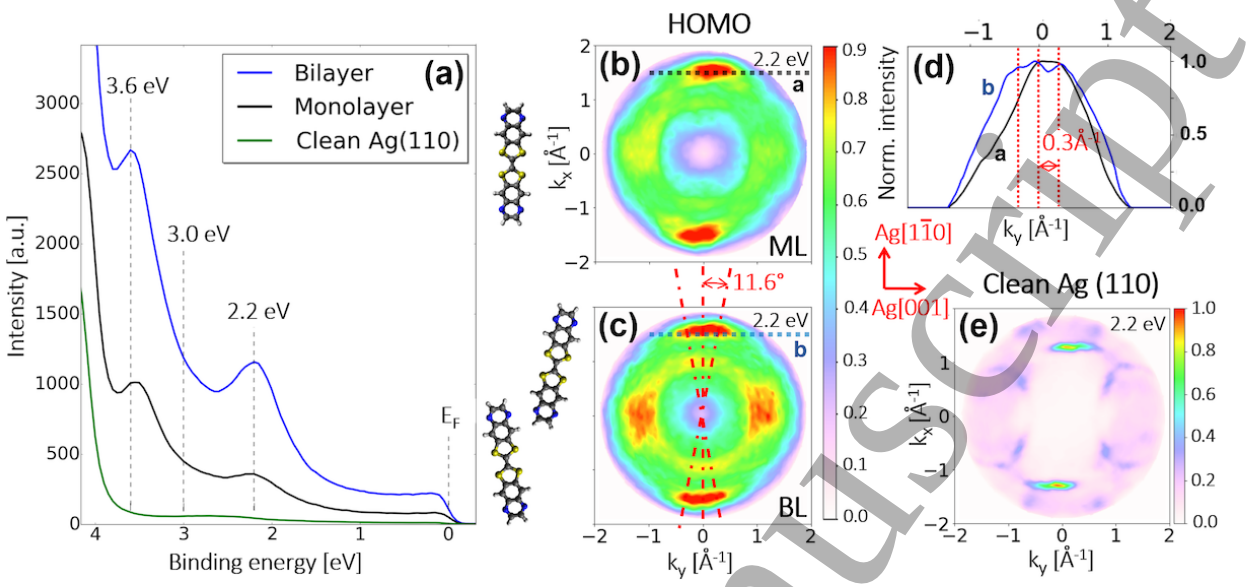

FIG. 4. Valence spectra and molecular orientation. (a) UPS of TTF-PYZ_2 ML and BL on Ag(110) and of the clean substrate. All spectra were measured at θ=50° and φ=0°. (b,c) PMM at HOMO binding energy (2.2 eV) of ML and BL with indication of molecular orientations (left). (d) Normalised intensity profile along the main feature in (b,c) at k_x=1.5 $Å^{-1}$. The broader BL profile (blue) can be attributed to the azimuthal rotation of the molecules in the second layer. The dashed lines indicate the theoretical maxima of the feature for the 3 orientations. (e) PMM of clean Ag(110) at 2.2 eV. The slight asymmetry with respect to the substrate mirror planes apparent in all PMMs is due to photoemission matrix element effects reflecting the orientation of the He-lamp outside the measurement-plane in the experiment.

Fig. 5(d) where vertical profiles along $k_y = 0$ are shown for both the experimental PMMs and the simulations.

Since there is no energy shift between molecules in the first and second layer, the BL signal always contains attenuated contributions from the first layer (ML). The effect of azimuthal rotation of the molecules already discussed for the HOMO PMM is also visible in case of the other states where it leads to a similar broadening of the features along this rotation. Interestingly, the seemingly very similar wave functions of HOMO-1 and HOMO-2 lead to quite different momentum distributions. This can easily be rationalised using symmetry arguments. The additional nodal plane perpendicular to the x-axis through the molecular centre changes the parity with respect to this plane. In this case, this leads to

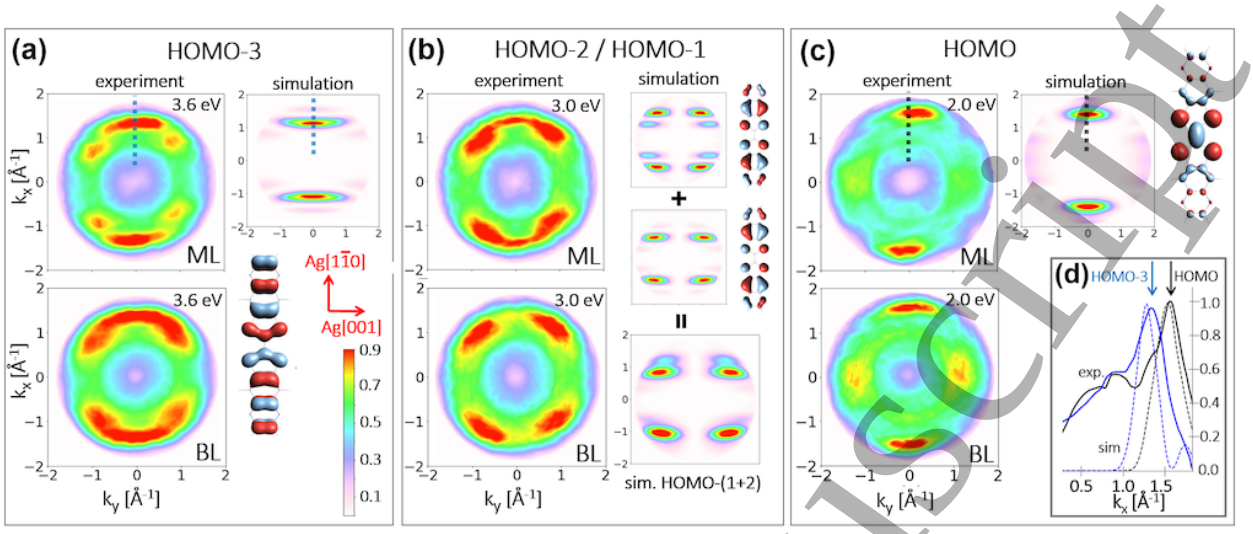

FIG. 5. Identification of molecular states. (a-c) Comparison between the measured PMM and simulations. The corresponding real space molecular orbitals are also shown. The measured PMM in (b) is the sum of two energetically close states (HOMO-2 and HOMO-1) that cannot be resolved in the experiment. All PMMs were normalized to the respective maximum intensities. The absolute intensities at all three energies are comparable, leading to similar contrast. (d) Normalised intensity profile for HOMO and HOMO-3 at k_y=0 Å^{-1}.

the additional features along k_x in the simulated momentum distributions. It has been shown before, that even in case of limited agreement between simulations and experiment, the molecular symmetry is always reproduced in the momentum distributions [20] and thus serves as reliable identifier of molecular states. The apparent node at $k_y = 0$ in the PMMs of HOMO-1/HOMO-2 (Fig. 5(b)) explains the absence of a peak for these states in the UPS spectrum (Fig. 4(a)) that was taken at this azimuthal orientation. The minimum along $k_y = 0$ is a direct consequence of the nodal plane along the long axis of the molecule in HOMO-1 and HOMO-2. Such nodal plane is not present in HOMO or HOMO-3 and thus there is no minimum at $k_y = 0$. For this reason, it is evident that the feature at 3.0 eV is an additional molecular state that cannot be explained by an overlap of the neighbouring HOMO-3 and HOMO states.

The lack of any discernible energy difference between corresponding states in the first and second layer indicates little interaction between the Ag substrate and the TTF-PYZ_2 molecules in terms of hybridisation or net charge transfer. The comparison further verifies the validity of the DFT-predicted orbital hierarchy and corroborates our earlier finding of

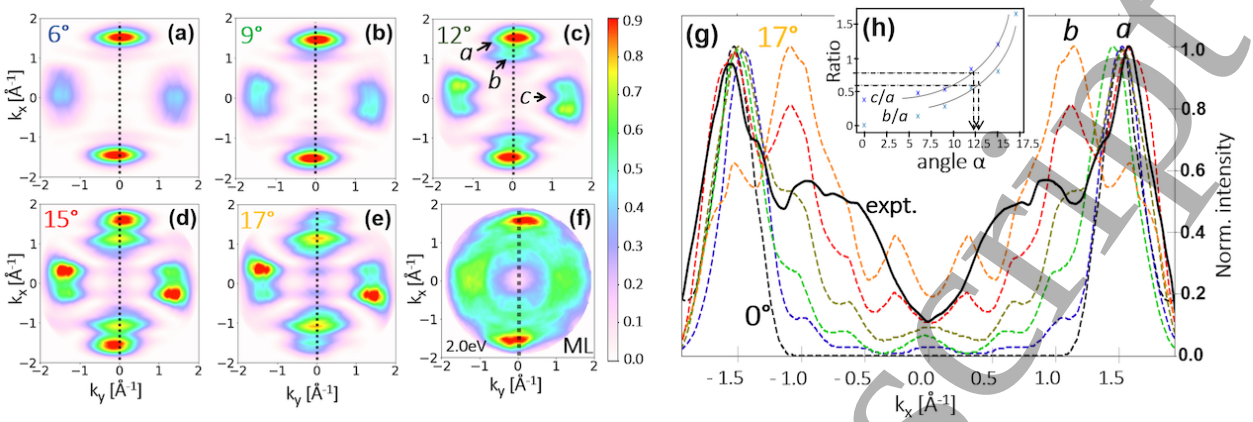

FIG. 6. (a-e) Simulated TTF-PYZ$_2$ HOMO PMM for different bending angles α. In (c) the main HOMO features are labeled. (f) Experimental HOMO PMM of the ML. (g) Normalized intensity profile of the simulations and experiment along the features a and b of the HOMO at $k_y = 0$ Å^{-1} (dashed lines). (h) Estimation of bending angle α.

weak interaction between the molecules and the substrate since all DFT calculations were performed on an isolated gas phase molecule.

C. Molecular geometry

One reason for the limited agreement between the experimental PMMs and the simulations is the bent geometry of the molecule as shown in Fig. 1(a.) The bending angle α is likely to change upon adsorption of the molecule due to interaction with the substrate. The IAC simulations depend strongly on the molecular geometry and we thus varied this bending angle to find the best match with the experiment. To do so, we employed the HOMO data as before for the verification of the azimuthal rotation in the second layer. The HOMO is most suitable for this purpose because its spectral features are well separated in energy from those of neighbouring molecular states.

Figure 6 shows simulated PMMs for different values of the bending angle α. This angle has a big influence on the ratios between the main HOMO feature ***a*** and the two features ***b*** and ***c*** indicated in Fig. 6(c). The increase of feature ***b*** relative to ***a*** can be seen in the intensity profiles shown in Fig. 6(g). We focus on the ML data because for higher coverage, the signal always contains contributions from both, first and second layer, since the HOMO level does not shift. Different substrate background intensities at these positions in k-space make the

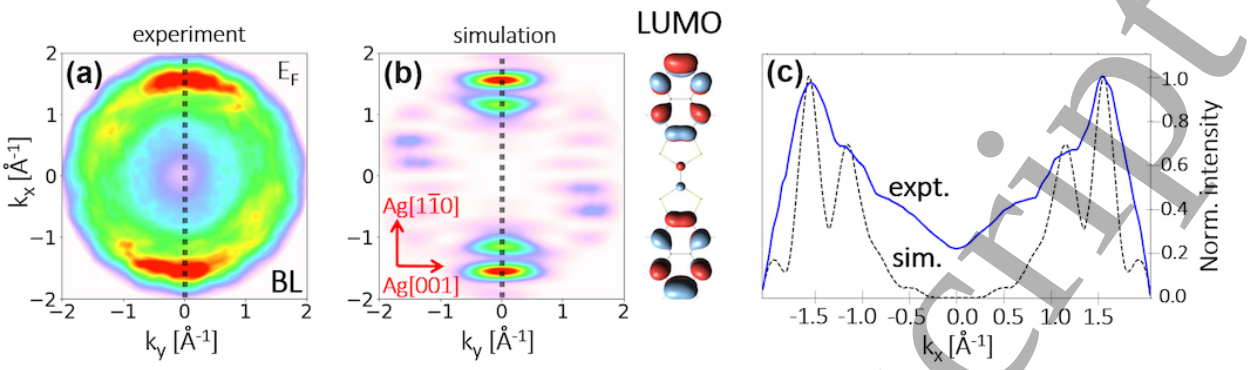

FIG. 7. (a) Experimental PMM of the BL at the Fermi energy. (b) Simulation of the 12° bent LUMO PMM along with the real space orbital. (c) Normalized intensity profile of the simulation and experiment along the LUMO at $k_y = 0$ Å^{-1} (dashed lines).

ratio coverage-dependent and lead to some uncertainty in the determination of the angle. Nevertheless, the experimental ratios can be estimated as $\boldsymbol{b}/\boldsymbol{a} = 0.63$ and $\boldsymbol{c}/\boldsymbol{a} = 0.78$. Based on these ratios, the bending angle is estimated by the interpolation shown in Fig. 6(h) to be $\alpha = 12.5 \pm 2°$ in the ML. This is similar to the bending found for TTF-PYZ_2 on NaCl [14]. Comparing the ML and BL data shown in Fig. 4(b/c), it can be seen that the $\boldsymbol{b}/\boldsymbol{a}$ and $\boldsymbol{c}/\boldsymbol{a}$ ratios are larger in the BL, indicating that the second layer molecules are bent slightly stronger, but still less than the free gas phase molecule in our DFT calculations ($\alpha = 17°$).

D. Electronic structure: charge-transfer and interactions

Naturally, when studying charge-transfer-complex molecules, the question of charge transfer comes to mind. Looking at the ML valence spectrum in Fig. 4(a), no distinct peak can be found between the TTF-PYZ_2 HOMO and E_F, which would be indicative of partial LUMO occupation. We notice though enhanced intensity in this region in the BL data. The PMM of a BL of TTF-PYZ_2 at the Fermi energy in Fig. 7, shows an angular distribution that closely resembles the simulation of the molecular LUMO. Interestingly, the intensity of LUMO features is stronger in the BL data than in the ML data. The lowering of the work function could be rationalised by charge transfer of the molecular HOMO to the substrate, which would be the opposite direction of transfer from the substrate into the LUMO. The

fact though that we see more pronounced charge transfer in the second layer hints towards intermolecular charge transfer, either between adjacent molecules in the same layer, or between the first and second molecular layer. The azimuthal rotation of the molecules in the second layer brings the acceptor and donor moieties of adjacent molecules in close proximity (see Fig. 3(e)). In the first layer, the molecules are oriented such that acceptor and donor functionalities are aligned and thus further apart from each other. The only slight modification of the molecular geometry upon adsorption indicates little interaction with the substrate and thus also supports the picture of intermolecular charge transfer.

IV. CONCLUSION

We investigated the charge-transfer-complex TTF-PYZ_2 on Ag(110) in a combined orbital tomography and LEED study. The molecules form a long-range ordered superstructure which is densely packed in the first and second layer. In the first layer, the long axis of the molecules is aligned with the Ag rows. In the second layer, the molecules are azimuthally rotated by $\sim 11.6°$. Four molecular states could be identified between E_F and the onset of the silver substrate *d*-bands. Detailed analysis of the photoelectron momentum maps (PMM) of these states confirms the molecular orientation deduced from the LEED data. A detailed simulation of the PMMs also enabled us to derive the bending angle of TTF-PYZ_2 on Ag(110). The found angle of 12.5° is slightly smaller than in the free molecule and comparable to findings of an earlier study for TTF-PYZ_2 adsorbed on NaCl [14]. Interestingly, while the latter study found two bent conformations of the molecules on Ag(110), we found only one boat (down) conformation with the TTF centre closer to the substrate. The PMM of a bilayer of TTF-PYZ_2 on Ag(110) at E_F indicates partial occupation of the molecular LUMO. Since this effect is more pronounced in the second layer, we conclude charge-transfer to occur between neighbouring molecules in the same layer (in-plane). Interaction between TTF-PYZ_2 and the Ag(110) substrate seems rather limited since no energy shift between molecular states in the first and second layer was observed and because the molecular geometry closely resembles the one of the free molecule. The observed high degree of long-range order in the LEED data can be largely attributed to intermolecular interactions. Yet the influence of the substrate is large enough to guide the molecules to adsorb along the Ag rows. The combination of orbital tomography with LEED is a powerful and efficient technique to

study both the adsorption geometry and the electronic structure of this interesting system.

CONFLICTS OF INTEREST

There are no conflicts to declare.

ACKNOWLEDGEMENTS

Financial support from the Swiss National Science Foundation (SNF) through NCCR-MUST and from the Deutsche Forschungsgemeinschaft (Projects SCHO1260/4-2 and RE1469/12-2) are gratefully acknowledged.

[1] Ferraris, J., Cowan, D., Walatka, V. t. & Perlstein, J. Electron transfer in a new highly conducting donor-acceptor complex. *Journal of the American Chemical Society* **95**, 948–949 (1973).

[2] D. Jerome, M. R., A. Mazaud & Bechgaard, K. Superconductivity in a synthetic organic conductor (tmtsf)2pf6. *J. Phvs. Lett.* **41**, L95 (1980).

[3] Elbing, M. *et al.* A single-molecule diode. *Proceedings of the National Academy of Sciences of the United States of America* **102**, 8815–8820 (2005).

[4] Pfattner, R. *et al.* Photo-induced intramolecular charge transfer in an ambipolar field-effect transistor based on a π-conjugated donor–acceptor dyad. *J. Mater. Chem. C* **1**, 3985–3988 (2013).

[5] Aviram, A. & Ratner, M. A. Molecular rectifiers. *Chemical Physics Letters* **29**, 277 – 283 (1974).

[6] Goetz, K. P. *et al.* Charge-transfer complexes: new perspectives on an old class of compounds. *Journal of Materials Chemistry C* **2**, 3065–3076 (2014).

[7] Bergkamp, J. J., Decurtins, S. & Liu, S.-X. Current advances in fused tetrathiafulvalene donor–acceptor systems. *Chemical Society Reviews* **44**, 863–874 (2015).

[8] Amacher, A. *et al.* A quinoxaline-fused tetrathiafulvalene-based sensitizer for efficient dye-sensitized solar cells. *Chem. Commun.* **50**, 6540–6542 (2014).

[9] Martín, N. Tetrathiafulvalene: the advent of organic metals. *Chem. Commun.* **49**, 7025–7027 (2013).

[10] Jia, H.-P. *et al.* Targeting π-conjugated multiple donor–acceptor motifs exemplified by tetrathiafulvalene-linked quinoxalines and tetrabenzovalenes: Synthesis, spectroscopic, electrochemical, and theoretical characterization. *Chemistry–An Asian Journal* **6**, 3312–3321 (2011).

[11] Goze, C. *et al.* Fused donor–acceptor ligands in ruii chemistry: Synthesis, electrochemistry and spectroscopy of [ru (bpy) 3- n (ttf-dppz) n](pf6) 2. *ChemPhysChem* **8**, 1504–1512 (2007).

[12] Leiggener, C. *et al.* Dual luminescence and long-lived charge-separated states in donor-acceptor assemblies based on tetrathiafulvalene-fused ruthenium (ii)-polypyridine complexes. *CHIMIA International Journal for Chemistry* **61**, 621–625 (2007).

[13] Wielopolski, M., Atienza, C., Clark, T., Guldi, D. M. & Martín, N. p-phenyleneethynylene molecular wires: Influence of structure on photoinduced electron-transfer properties. *Chemistry–A European Journal* **14**, 6379–6390 (2008).

[14] Schuler, B. *et al.* Contrast formation in kelvin probe force microscopy of single π-conjugated molecules. *Nano letters* **14**, 3342–3346 (2014).

[15] Puschnig, P. *et al.* Reconstruction of Molecular Orbital Densities from Photoemission Data. *Science* **326**, 702–706 (2009).

[16] Weiß, S. *et al.* Exploring three-dimensional orbital imaging with energy-dependent photoemission tomography. *Nature Communications* **6**, 8287 EP – (2015).

[17] Kliuiev, P., Latychevskaia, T., Osterwalder, J., Hengsberger, M. & Castiglioni, L. Application of iterative phase-retrieval algorithms to arpes orbital tomography. *New Journal of Physics* **18**, 093041 (2016).

[18] Kliuiev, P. *et al.* Combined orbital tomography study of multi-configurational molecular adsorbate systems. *Nature Communications* **10**, 5255 (2019).

[19] Goldberg, S., Fadley, C. & Kono, S. Photoelectric cross-sections for fixed-orientation atomic orbitals: Relationship to the plane-wave final state approximation and angle-resolved photoemission. *Solid State Communications* **28**, 459 – 463 (1978).

[20] Puschnig, P. *et al.* Orbital tomography: Deconvoluting photoemission spectra of organic molecules. *Physical Review B* **84**, 235427 (2011).

[21] Lüftner, D. *et al.* Imaging the wave functions of adsorbed molecules. *PNAS* **111**, 605–10 (2014).

[22] Kliuiev, P. *et al.* Algorithms and image formation in orbital tomography. *Phys. Rev. B* **98**, 085426 (2018).

[23] Grobman, W. D. Angle-resolved photoemission from molecules in the independent-atomic-center approximation. *Physical Review B* **17**, 4573 (1978).

[24] Sitter, H., Draxl, C. & Ramsey, M. *Small Organic Molecules on Surfaces: Fundamentals and Applications* (Springer Science & Business Media, 2013).

[25] Greif, M., Castiglioni, L., Becker-Koch, D., Osterwalder, J. & Hengsberger, M. Acquisition of photoelectron diffraction patterns with a two-dimensional wide-angle electron analyzer. *Journal of Electron Spectroscopy and Related Phenomena* **197**, 30 – 36 (2014).

[26] Liebsch, A. Theory of photoemission from localized adsorbate levels. *Phys. Rev. B* **13**, 544–555 (1976).

[27] Hasegawa, S. *et al.* Molecular orientation in thin films of bis(1,2,5-thiadiazolo)-p-quinobis(1,3-dithiole) on graphite studied by angle-resolved photoelectron spectroscopy. *Phys. Rev. B* **48**, 2596–2600 (1993).

[28] Fujikawa, T. & Arai, H. Many-body theory of core-level photoemission by keldysh green's functions. *Journal of Electron Spectroscopy and Related Phenomena* **123**, 19 – 46 (2002).

[29] Grimm, M. *et al.* Molecular orbital imaging beyond the first monolayer: Insights into the pentacene/ag(110) interface. *Phys. Rev. B* **98**, 195412 (2018).

[30] Frisch, M. J. *et al.* Gaussian 09, Revision B.01. Gaussian Inc. Wallingford CT (2010).

[31] Oura, K., Lifshits, V., Saranin, A., Zotov, A. & Katayama, M. *Surface Science: An Introduction* (Springer-Verlag Berlin Heidelberg, 2003).